Foil Bearing Design Guidelines for Improved Stability

Foil Bearing Design Guidelines for Improved Stability

J. Schiffmann[1]
e-mail: jurg.schiffmann@epfl.ch

Z. S. Spakovszky
e-mail: zolti@mit.edu

Gas Turbine Laboratory,
Massachusetts Institute of Technology,
Cambridge, MA 02139

Experimental evidence in the literature suggests that foil bearing-supported rotors can suffer from subsynchronous vibration. While dry friction between top foil and bump foil is thought to provide structural damping, subsynchronous vibration is still an unresolved issue. The current paper aims to shed new light onto this matter and discusses the impact of various design variables on stable foil bearing-supported rotor operation. It is shown that, while a time domain integration of the equations of motion of the rotor coupled with the Reynolds equation for the fluid film is necessary to quantify the evolution of the rotor orbit, the underlying mechanism and the onset speed of instability can be predicted by coupling a reduced order foil bearing model with a rigid-body, linear, rotordynamic model. A sensitivity analysis suggests that structural damping has limited effect on stability. Further, it is shown that the location of the axial feed line of the top foil significantly influences the bearing load capacity and stability. The analysis indicates that the static fluid film pressure distribution governs rotordynamic stability. Therefore, selective shimming is introduced to tailor the unperturbed pressure distribution for improved stability. The required pattern is found via multiobjective optimization using the foil bearing-supported rotor model. A critical mass parameter is introduced as a measure for stability, and a criterion for whirl instability onset is proposed. It is shown that, with an optimally shimmed foil bearing, the critical mass parameter can be improved by more than two orders of magnitude. The optimum shim patterns are summarized for a variety of foil bearing geometries with different L/D ratios and different degrees of foil compliance in a first attempt to establish more general guidelines for stable foil bearing design. At low compressibility ($\Lambda < 2$), the optimum shim patterns vary little with bearing geometry; thus, a generalized shim pattern is proposed for low compressibility numbers. [DOI: 10.1115/1.4007759]

Introduction

Over the past three decades, foil bearings have found a wide range of applications, such as in air cycle refrigeration units [1], microturbine generators [2,3], and turboexpanders for cryogenic application [4]. Foil bearings allow oil-free operation, as lubrication is provided by a gas film. The typical foil bearing consists of a thin top foil supported by a corrugated bump foil. The bump foil structure acts like a spring, making the top foil compliant. Dry friction resulting from relative motion between the foils provides structural damping. The leading edge of the top foil is free, whereas the trailing edge is typically welded to the bearing sleeve. By tuning the support stiffness in the circumferential direction and by introducing multistage bump foils, Heshmat [5] demonstrated relatively large load capacities (for example, nondimensional loads, F, of 6.7). In addition, the development of coatings has ensured low starting torque and limited wear during startup and shutdown and allows operation under heavy loads and at high temperatures [6].

Nature of the Issues. Subsynchronous rotor motion is a long-standing issue, and a number of publications in the literature give recurring evidence of such vibrations in foil bearing-supported rotors [5,7–9]. Subsynchronous vibration in fluid film bearings is a well understood phenomenon also known as bearing whirl. The motion can result from cross-coupled fluid film forces leading to vibration at the rotor natural frequency. Although foil bearing-supported rotors are known to operate reliably with small subsynchronous limit cycles, the consequences can be rotor failure or premature wear and fatigue. To avoid this undesirable vibration, damping can be provided by the fluid film itself or through external means, such as squeeze film dampers or O-rings. It is conjectured in the literature that the dry friction between the top foil and the bump foil provides structural damping, enhancing bearing rotordynamic stability [6,10]. To improve the bearing frictional characteristics, Heshmat et al. [10] coated the adjacent foil surfaces with copper and showed reduced rotor orbits. Lee et al. [11] added a viscoelastic foil between the bump and the top foil. Test results showed attenuated orbits for operation at the bending-critical speed. San Andrés et al. [12,13] proposed to replace the bump foil with a metal mesh. The experiments provided stiffness coefficients similar to those of bump foil-supported bearings and demonstrated improved structural damping, reducing the orbit amplitude.

San Andrés and Kim [14] conjectured that the nonlinear support stiffness of the bump foil contributes to subsynchronous vibrations. Rubio and San Andrés [15] determined the stiffness of a bump-type foil bearing at zero rotational speed and showed that the stiffness increased with eccentricity. By applying the measured nonlinear stiffness and assuming that the combined stiffness of the fluid film and the bearing support is dominated by the bump foil structure [16], Kim and San Andrés performed a nonlinear rotordynamic analysis by numerically integrating the governing differential equations. The analysis showed subsynchronous vibration, suggesting that the foil bearing is governed by the bump foil structure and that the undesired motion is due to its nonlinear stiffness. This paper shows that the onset speed of instability computed by a linear rotordynamic model coupled with a reduced order foil bearing model is in agreement with both the onset speed predicted by the nonlinear rotordynamic analysis and with experimental data.

The current paper investigates the role of Coulomb friction and the location of the axial feed line of the top foil in subsynchronous vibration. Furthermore, the so-called "selective shimming" is introduced as a means to tailor the fluid film pressure to significantly delay the whirl onset.

Goals and Objectives. The goal of the investigation is to define a set of unified design guidelines for stable foil bearing-supported

[1]Currently at Ecole Polytechnique Fédérale de Lausanne, CH-1015 Lausanne, Switzerland.

Contributed by the Tribology Division of ASME for publication in the JOURNAL OF TRIBOLOGY. Manuscript received February 10, 2012; final manuscript received September 8, 2012; published online December 20, 2012. Assoc. Editor: Luis San Andres.

rotor operation. The objectives are to: (1) conceive a comprehensive model for foil bearing-supported rotors based on existing, state-of-the-art component models; (2) investigate the role of Coulomb friction in subsynchronous vibration; (3) quantify the impact of the axial foil bearing feed line orientation on static load; and (4) characterize the stability of foil bearing-supported rotors and define the conditions under which stable operation is guaranteed.

Scope of the Paper. The technical approach is based on an integrated rotordynamic model for foil bearing-supported rotors. The foil bearing model by Kim and San Andrés [17] is implemented. The model is able to estimate the static load capacity and the dynamic stiffness and damping coefficients as a function of bearing geometry and operation conditions. Then, the foil bearing model is coupled with a linear, rigid body rotordynamic model, implementing an extension of the spectral analysis approach by Pan [18] and Pan and Kim [19]. The analysis estimates the whirl speed map and the corresponding stability map of a rotordynamic system where stiffness and damping are not only dependent on the rotational speed but also on the excitation frequency. This is generally the case for fluid film bearings with a compressible lubricant. The integrated model is then used to assess the hypothesis by comparing the simulation results with available experimental data. Furthermore, a numerical sensitivity analysis is carried out to identify the key parameters governing subsynchronous vibration. It is shown that, for lightly loaded bearings, structural damping has a negligible effect on the onset of subsynchronous vibration. So called "selective shimming" is then pursued by introducing shims with variable thickness around the bearing circumference. The idea is that, by selective shimming, the unperturbed pressure field, which governs the stiffness and damping characteristics, is altered so as to increase the stability threshold.

Using a critical mass parameter, the selective shim distribution is optimized to maximize the stability threshold for a range of length-to-diameter ratios and static loads. The results are generalized with the goal to identify improved bearing configurations for a given application.

Integrated Model Description

Foil Bearing Model. A foil bearing model is required to estimate the static load capacity and the dynamic stiffness and damping coefficients as a function of bearing geometry and operating conditions, such as rotational speed, excitation frequency, static eccentricity, and lubricant properties. Figure 1 illustrates the layout of a typical bump foil bearing and introduces the nomenclature used in this paper.

A wide range of tools for estimating foil bearing performance are available in the literature. A typical approach is to model the compliance of the bump foil as an equivalent stiffness distributed around the bearing circumference [17,20,21]. More comprehensive models include the elastic deformation of the top foil [22] and of the bump foil [23,24]. Kim and San Andrés [17] use an equivalent bump foil stiffness model and assume the top foil does not deform [25]. The comparison with experimental data suggests that more elaborate models offer little improvement in accuracy of the predicted stiffness and damping coefficients. Thus, a similar approach is used here.

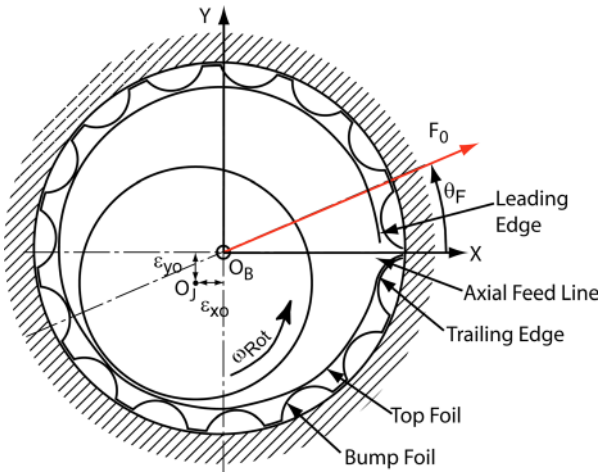

Fig. 1 Bump foil gas bearing nomenclature

The pressure in the fluid film is governed by the Reynolds equation, which for an isothermal, ideal gas in its nondimensional form can be written as

$$\partial_\theta\left[PH^3\partial_\theta P\right] + \partial_z\left[PH^3\partial_z P\right] = \Lambda\partial_\theta(PH) + \sigma\partial_\tau(PH) \tag{1}$$

with

$$H = 1 + \varepsilon_x\cos(\theta) + \varepsilon_y\sin(\theta) + \alpha(P-1)$$
$$\alpha = \frac{p_a}{CK_B(1+i\gamma)} \tag{2}$$

The set of equations can be solved by a perturbation method. Small perturbations about a statically off-set rotor are introduced to yield partial differential equations for the zeroth and first order pressure perturbations. The partial differential equations are solved using the finite element method by Faria and San Andrés [26] and Faria [27]. Integration of the zeroth order pressure field yields the static force components for a given static eccentricity ε_{x0}, ε_{y0}. The integration of the two first order terms of the pressure field determines the direct and the cross-coupled stiffness and damping coefficients. It is important to note that the static force coefficients depend on static eccentricity and rotational speed, whereas the dynamic bearing coefficients are governed by the zeroth order pressure distribution plus excitation frequency, which might be different from the shaft rotational frequency. Kim and San Andrés [17] account for mechanical dissipation losses generated by Coulomb friction between the foils via a structural loss coefficient, γ. Typical bump-type foil bearings yield empirical structural loss coefficients ranging from 0.05 to 0.2 for nondimensional static loads of 0.028 to 0.14 [28].

The foil bearing under investigation is composed of a single-leaf top foil that is loosely laid upon a bump foil. Both are spot-welded to the bearing sleeve at the trailing edge only. Hence, the top foil may lift off if subambient pressures are generated within the bearing fluid film. The top foil in lift-off mode floats between the rotor and the bump foil and adjusts the fluid film distribution such as to avoid subambient fluid film pressures. Considering the fluid film evolution in the angular direction, the top foil is assumed to stop floating only when the top foil gets forced into a converging aerodynamic wedge. For rotor eccentricities towards the axial feed line, the top foil may be in floating mode for a very large angular section, thus limiting load capacity.

Although Kim and San Andrés [29] show that bearing side pressurization delays the whirl speed onset, it should be mentioned that the predictions in the present paper are performed without bearing side feed pressurization.

Whirl Speed and Stability Maps. An important feature of gas-lubricated bearings is that the bearing properties are not only a function of rotor speed but also depend on excitation frequency. This needs to be taken into account in the stability assessment. The approach here is based on Pan's spectral analysis method [18] extended by Schiffmann and Favrat [30–32]. The rigid-body rotordynamic system is shown in Fig. 2 and described by

$$[M]\ddot{\vec{q}} + [C]\dot{\vec{q}} + [K]\vec{q} = \vec{f} \tag{3}$$

where $[M]$ is the system inertia and $[K]$ the bearing stiffness coefficients. $[C]$ is composed of the bearing damping coefficients and

gyroscopic effects. The rotor geometry and properties are described in terms of mass, m_{Rot}, polar and transverse rotor inertia, J_P and J_T, and of the location of the bearing midplanes relative to the rotor center of gravity, l_a and l_b. Equation (2) yields an eigenvalue problem with eigenvalues

$$s_j = \lambda_j + i\Omega_j\omega_{\text{Rot}} \tag{4}$$

where the imaginary part $\omega_j = \Omega_j\omega_{\text{Rot}}$ is the damped natural frequency of the whirl motion and λ_j the corresponding damping coefficient. It is common practice to quantify rotor stability using the logarithmic decrement defined as

$$\Gamma_j = -\lambda_j \frac{2\pi}{\Omega_j\omega_{\text{Rot}}} \tag{5}$$

Stable operation requires $\Gamma > 0$. To determine the whirl speed and the stability map of a gas bearing-supported rotor, the system is excited over a range of frequencies, $\omega_{Ex} = \Omega\omega_{\text{Rot}}$, while keeping the rotor speed fixed. A rotor natural frequency is determined when the estimated whirl frequency coincides with the excitation frequency for a particular rotational speed. This is carried out for Ω ranging from 0 to 3. It can be shown that, for higher whirl ratios, the bearing properties reach asymptotic values (Pan and Kim [19]). It is emphasized that, in this particular analysis, neither external vibrations nor seal forces have been considered.

Nondimensional Stability Criterion. A compact description of stability was proposed by Pan [18], Pan and Kim [19], and Lund [33] by characterizing the stability threshold through a nondimensional critical mass parameter. The governing equations for cylindrical motion are

$$\begin{aligned} &\left[M_{\text{CYL}}s^2 + Z_{\text{CYL}}\right]\vec{q}e^{st} = \vec{0} \\ &M_{\text{CYL}} = \begin{bmatrix} m_{\text{Rot}} & 0 \\ 0 & m_{\text{Rot}} \end{bmatrix} \end{aligned} \tag{6}$$

where m_{Rot} is the rotor mass and Z_{CYL} is the translational system impedance, which includes bearing stiffness and damping coefficients. Diagonalization of Z_{CYL}, where the two diagonal terms become $z_{\text{CYL}-j} = u_{\text{CYL}-j} + iv_{\text{CYL}-j}$, yields the condition for neutral stability ($v_{\text{CYL}-j} = 0$ at $\Omega_{\text{Crit}-j}$). The corresponding critical mass m_{Crit} is then given by $u_{\text{CYL}-j}/(\Omega_{\text{Crit}-j}\omega_{\text{Rot}})^2$. In this paper, a nondimensional form of the critical mass for cylindrical motion is introduced as follows:

$$M_{\text{Crit}-j} = m_{\text{Crit}}\frac{p_a}{\mu^2 L}\left(\frac{C}{R}\right)^5 = 72\frac{u_{\text{CYL}-j}\dfrac{C}{P_a DL}}{\Omega^2_{\text{Crit}-j}\Lambda^2} \tag{7}$$

Applying the same procedure for the rotor-tilting motion, the critical transversal inertia can be found in nondimensional form.

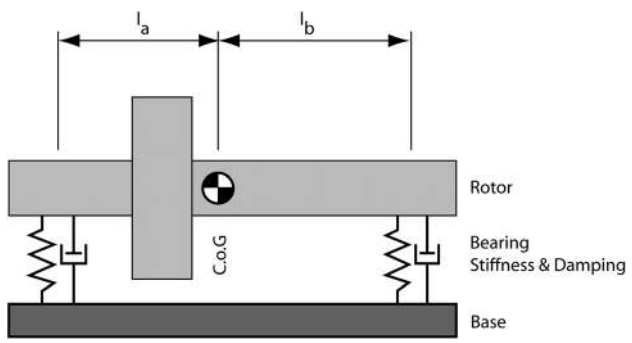

Fig. 2 Rotordynamic model for rigid body analysis

This parameter governs the stability for conical rotor motions and includes the gyroscopic moments

$$I_{\text{Crit}-j} = 72\frac{u_{\text{CON}-j}\dfrac{C}{P_a \text{DL}}}{\Lambda^2\left(\Omega^2_{\text{Crit}-j} - \dfrac{J_P}{J_T}\Omega_{\text{Crit}-j}\right)} \tag{8}$$

The rotor system impedance matrix for conical motion can be expressed in terms of the translational impedance as

$$z_{\text{CON}} = z_{\text{CYL}}l^2\left[\zeta^2 + (1-\zeta)^2\right] \tag{9}$$

where l is the distance between the two journal locations and ζ the center of gravity relative to the two bearing midplanes. The combination of Eqs. (8) and (9) yields

$$I_{\text{Crit}} = M_{\text{Crit}}\frac{l^2\left[\zeta^2 + (1-\zeta)^2\right]}{\left(1 - \dfrac{J_P}{J_T}\dfrac{1}{\Omega_{\text{Crit}}}\right)} \tag{10}$$

Note that the denominator can be negative. In this case, there is no conical resonance at the critical whirl ratio and the rotor undergoes a stable gyroscopic precession.

The relationship between the system tilting and translational impedance implies that the critical inertia can be expressed as a function of the critical mass. Furthermore, the critical mass parameter and the corresponding critical whirl speed ratio for a single bearing determine the translational and tilting stability threshold of a given rotor. The nondimensional critical mass concept will thus be used to establish stability design guidelines.

Model Limitations. The stiffness and damping coefficients obtained by the foil bearing model are not suitable for estimating large orbits resulting from a significant unbalance, since the approach is based on small perturbations in bearing properties. The model is however adequate to perform a rotordynamic stability analysis around a given static eccentricity not limited to small values. The analysis thus captures small orbits around a static eccentricity, and while it allows one to estimate the onset of instability, it cannot capture the evolution of the rotor orbit after instability onset. In addition, the foil bearing model uses a structural damping coefficient which accounts for material hysteresis and dry friction. While this is a convenient and commonly used model, it is a limited representation of these phenomena, because the loss coefficient assumes sinusoidal motion and is based on the average dissipation work over one period of motion. Therefore, it cannot capture dry friction-related phenomena, such as discontinuous forces and lockup.

Further, the bump foil stiffness is assumed uniform, constant, and independent of neighboring bumps. The top foil cannot flex between two bumps, but follows the deformation of the bump foil. In San Andrés and Kim [22], the top foil is modeled either as a simple beam or as a flat shell. The one-dimensional beam model agrees with experimental data for nondimensional loads below 0.35. For normalized loads greater than 1.0, the simple model overpredicts the direct stiffness by approximately 5% [22]. In conclusion, the simple model is adequate for lightly loaded bearings, where the static load corresponds to the shaft weight only.

It should further be noted that the prediction of the bearing characteristics is based on the assumption of perfect geometry. Hence, the foil bearing model does not account for manufacturing and assembly imperfections.

Prediction Results and Sensitivity Analysis

Model Prediction versus Published Experimental Data. In order to validate the model, the method was implemented for the

Table 1 Rotor and bearing parameters from Refs. [14], [34], and [35] used in the sensitivity analysis

Foil bearing parameters	
D (mm)	38.1
L/D (–)	1
C (μm)	35.5
α (–)	0.67
γ (–)	0.14
Rotor parameters	
m_{Rot} (kg)	0.98
J_T (kgm^2)	3.71×10^{-3}
J_P (kgm^2)	2.24×10^{-4}

rotor and bearing geometry reported in San Andrés and Kim [14,34] and San Andrés et al. [35], where experimental data is available. Next, a sensitivity analysis was carried out to investigate the effects of static load, structural damping, and bearing compliance on rotordynamic performance. The geometric parameters of this rotor-bearing system are summarized in Table 1. According to Ref. [14], the rotor center of gravity was assumed to be equidistant from the two supporting bearings.

The experimental data shows that subsynchronous vibrations appear at a rotor speed of approximately 12 krpm, which corresponds to a compressibility number of $\Lambda = 0.39$ for this bearing. The measured whirl speed ratio, Ω, at onset is 0.5. Using the integrated rotor-bearing model, the estimated whirl speed map for conical and cylindrical modes and the corresponding logarithmic decrement for forward and backward whirl are given in Fig. 3. The linear rotordynamic model predicts instability onset at a compressibility number of $\Lambda = 0.43$ with a whirl ratio of 0.5. The corresponding critical mass is plotted as a function of the compressibility number in Fig. 4. The critical mass decreases with increasing compressibility numbers, and instability is reached at $\Lambda = 0.43$.

Using the integrated model, the computed compressibility number and the whirl speed ratio at instability onset are in good agreement with both the experimental measurements and the nonlinear rotordynamic analysis by San Andrés and Kim [14]. Thus, the integrated model, which is based on a linearized approach and does not assume nonlinear stiffness characteristics, captures the experimentally measured whirl onset. It is worth mentioning that this is in agreement with the results by San Andrés et al. [35].

Role of the Axial Feed Line Orientation. Single leaf foil bearings generally feature an axially slit top foil that imposes an ambient pressure boundary condition which leads to bearing anisotropy. To investigate the role of the axial feed line orientation on bearing performance, a constant static load at varying angles was applied to the reference rotor-bearing system (Table 1). Figure 5 presents the resulting static eccentricity for different load levels. The radial lines connecting the orbits represent isoloading angles, demonstrating that increased static loads reduce the attitude angle. This implies that the direct stiffness increases more rapidly with eccentricity than the cross-coupled terms, suggesting improved rotordynamic performance. Furthermore, it is shown that, based on the implemented model, the estimated load capacity vanishes for static eccentricities toward the axial feed line. At these operating conditions, no fluid film wedges are generated due to lift-off of the top foil resulting from subambient fluid film pressures. As a consequence, contact between rotor and top foil occurs, potentially limiting bearing life. The range of critical load angles increases with load. At a low load ($F = 0.033$), angles between 150 deg and 190 deg should be avoided. For loads one order of magnitude larger, the critical range extends from 100 deg to 230 deg. This analysis suggests that the load capacities reported in the literature in excess of

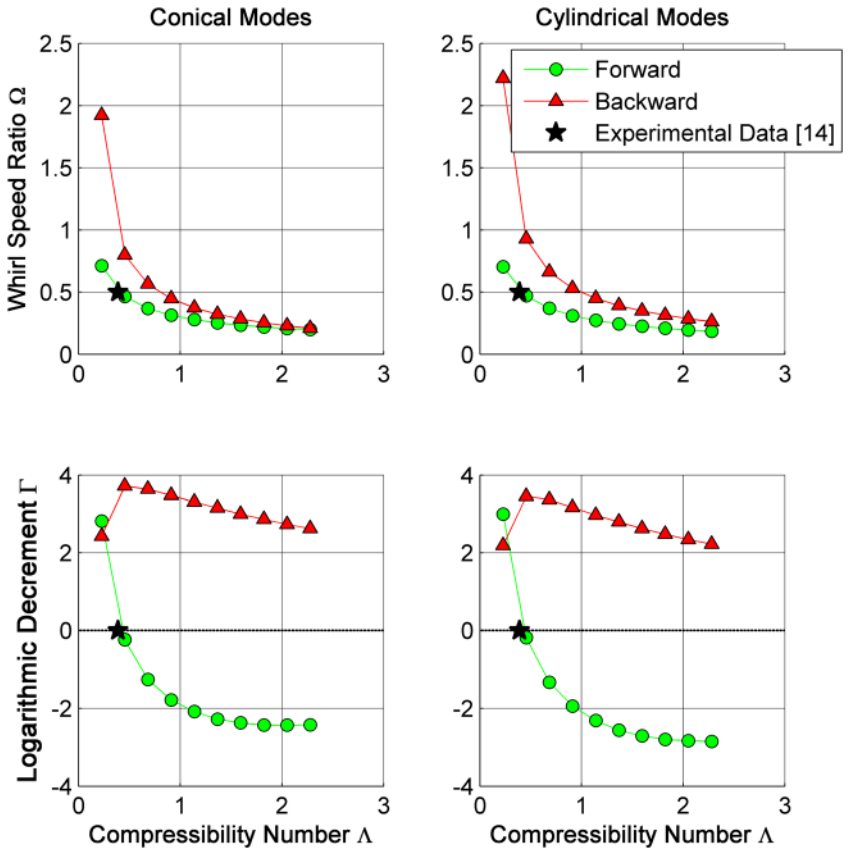

Fig. 3 Whirl speed map for cylindrical and conical modes for the reference rotor-bearing system (Table 1): onset of instability occurs at $\Lambda = 0.43$

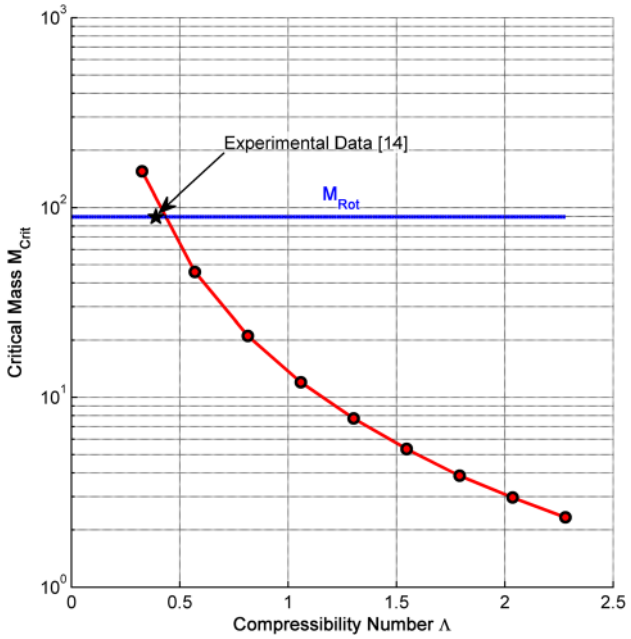

Fig. 4 Critical mass for reference rotor-bearing system (Table 1): onset of instability occurs at $\Lambda = 0.43$

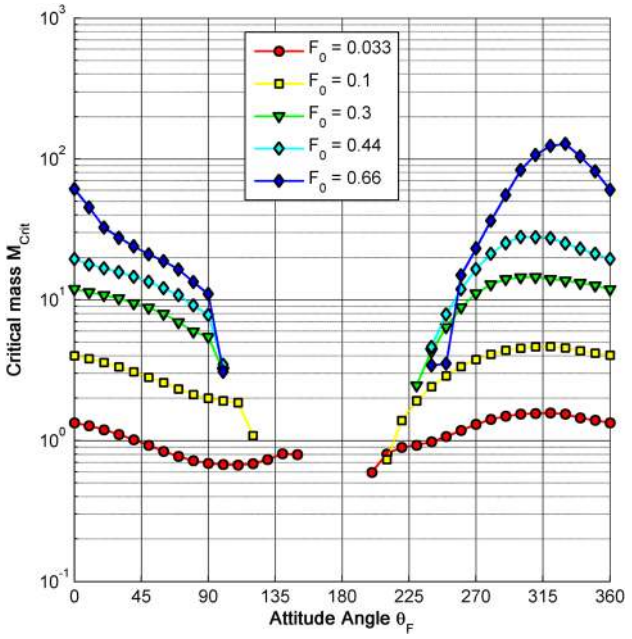

Fig. 6 Critical mass as a function of attitude angle and amplitude for reference bearing (Table 1) operating up to $\Lambda = 4$

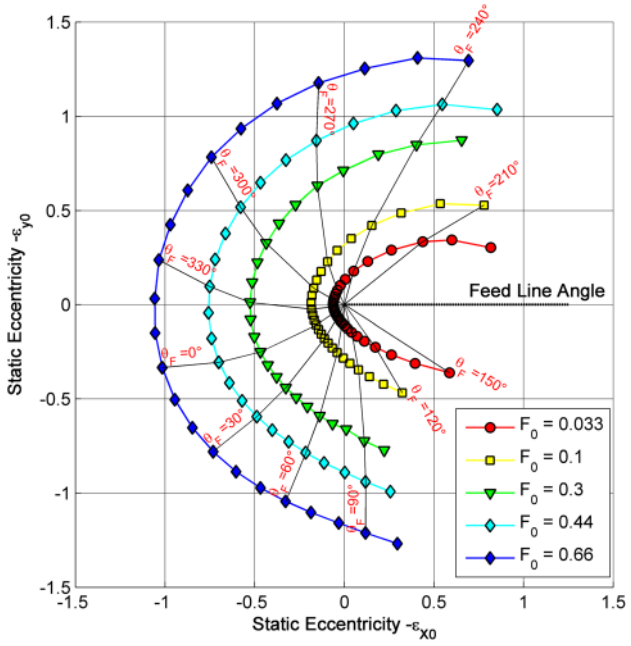

Fig. 5 Static eccentricity as a function of attitude angle and amplitude for reference journal bearing (Table 1) operating at $\Lambda = 4$

6.7 are certainly feasible [5], but only within a limited range of attitude angles.

Figure 6 depicts the evolution of the minimum critical mass as a function of load angle for bearing compressibility numbers Λ up to 4. The implication is that the rotordynamic performance is significantly affected by both static load amplitude and attitude angle. At low bearing loads ($F = 0.033$), the critical mass varies by a factor of three as a function of the load orientation. Increasing the static load by an order of magnitude increases the critical mass by the same ratio. Note that the critical mass decreases rapidly for loads displacing the rotor towards the axial feed line and that a load angle around 320 deg yields improved rotordynamic performance, independent of the load amplitude. It can be shown that, for other compressibility numbers, the qualitative behavior is similar.

In conclusion, the results suggest that foil bearing anisotropy due to the axial feed line orientation strongly affects bearing performance and needs to be taken into account in the design process, especially for rotors required to operate at any attitude angle.

Role of Compliance and Structural Damping. A numerical sensitivity analysis was also performed to investigate the effect of compliance and structural damping on rotordynamic performance. Figure 7 presents the critical mass of the reference bearing (Table 1) as a function of compressibility, static load, and bearing compliance. In this investigation, no structural damping was considered. The results suggest that decreasing the bearing compliance is beneficial for stability (improved critical mass), but tuning the compliance has little effect on stability compared to increasing the static load. It is important to note that the limiting case of zero compliance is not to be compared with a rigid cylindrical bearing, since asymmetry is introduced by both the axial feed line and the top foil lift-off resulting from diverging aerodynamic wedges.

Figure 8 shows the critical mass of the same bearing as a function of compressibility, static loads, and structural damping for a compliance of $\alpha = 0.67$. The results suggest that structural damping has a marginal role in rotordynamic performance (critical mass), especially at low loads. At increased loads and low compressibility, the effect of structural damping is somewhat increased. It is however suggested that improving structural damping for lightly loaded bearings is not sufficient to significantly delay the *onset* of subsynchronous whirl, although structural damping is known to decrease limit cycle subsynchronous vibration amplitude [11]. Further, it is emphasized that the present results are in agreement with data published by Kim et al. [36], although the present analysis only estimates the whirl onset, but not the rotor orbit thereafter. Using a time-domain simulation and solving the Reynolds equation and the rotor equations of motion simultaneously, Kim et al. show that structural damping has no effect on whirl onset speed.

In summary, the results show that increasing the static load and decreasing the bearing compliance seem to be the most efficient means to improve the rotordynamic performance, i.e., to delay the whirl onset. Static load affects the fluid film thickness and the

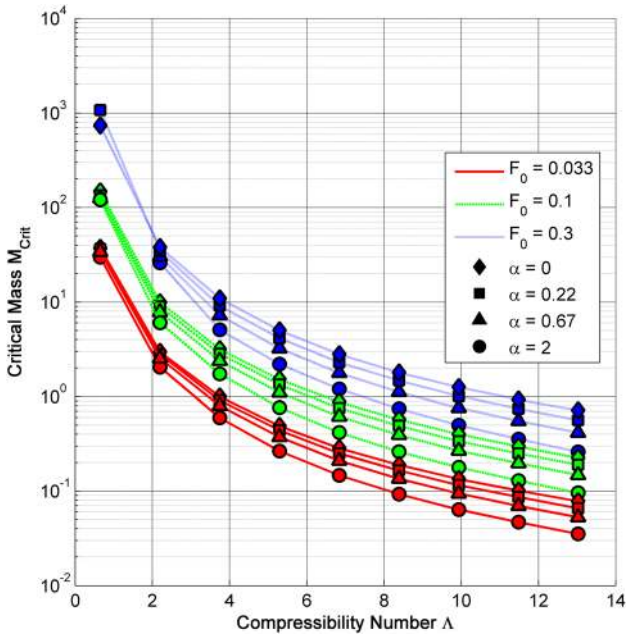

Fig. 7 Critical mass as a function of compressibility, static load, and compliance for reference bearing (Table 1) with no structural damping

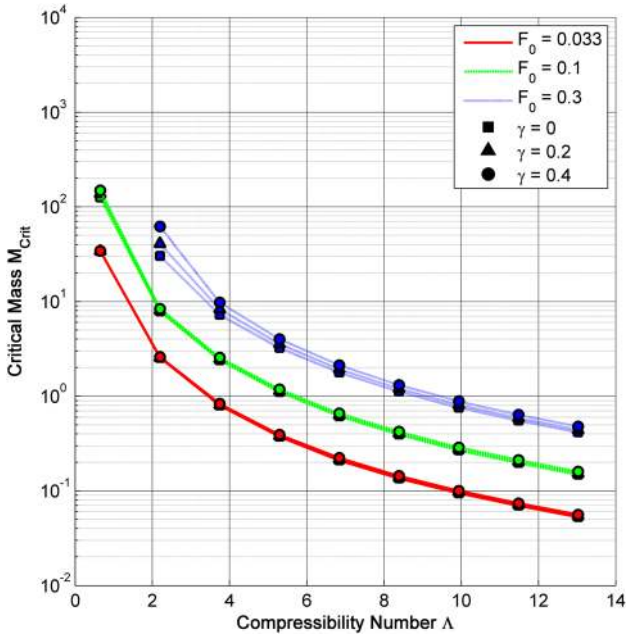

Fig. 8 Critical mass as a function of compressibility, static load, and structural damping for reference bearing (Table 1) at $\alpha = 0.67$

unperturbed pressure distribution such that the ratio between cross-coupled and direct coupled properties is decreased, yielding improved rotordynamic performance. It can thus be concluded that controlling the static pressure distribution is important to improve stability.

Selective Shimming

In most applications, the bearing is loaded via the rotor weight only and adding a controlled static load to the rotating shaft without extra complexity is challenging. Thus, it is common practice to add shims between the bump foil and the bearing sleeve to tailor the bearing pressure distribution. Kim and San Andrés [34] investigated the effect of three identical, equally distributed shims on a test rotor with subsynchronous vibration [35]. This showed that the shims delay the onset of the subsynchronous vibrations and decrease the motion amplitudes due to an increase in direct coupled stiffness resulting from the lobing effect. Both Kim et al. [9] and Sim et al. [37] repeated the same test on a turbo-charger rotor and drew the same conclusion. These experimental investigations suggest that shimming can improve the rotordynamic performance. However, the applied shimming pattern was not able to completely avoid subsynchronous vibrations.

In this paper, so called "selective" shimming is pursued by introducing shims with variable thickness around the bearing circumference. The idea is to tailor the fluid film pressure distribution so as to increase the bearing stability threshold. The required pattern is found via multiobjective optimization using the integrated rotor-bearing model and the reference rotor-bearing system (Table 1). It is assumed that the bearings are loaded through the rotor weight ($\theta_F = 0$ deg) and operate in a range of compressibility numbers of $\Lambda = 0.23$–3.2. The variables to be optimized are six equally distributed, individual, normalized, shim thicknesses. Each individual shim results in a local sinusoidal fluid film restriction that extends 72 deg in both angular directions. Mathematically, the optimization can be formulated as follows:

$$\max(\Gamma), \min(\bar{\varepsilon}_S)$$
$$n_S = 6$$
$$\phi_S = [0 \text{ deg}, 72 \text{ deg}, 144 \text{ deg}, 216 \text{ deg}, 288 \text{ deg}, 360 \text{ deg}]$$
$$\varepsilon_{S-i} \in [0 - 0.9]$$
$$\Lambda = [0.23 - 3.2]$$

where $\phi_S = 0$ deg corresponds to the open-ended leading edge of the top foil and $\phi_S = 360$ deg to the spot-welded trailing edge. The compressibility number Λ for shimmed bearings is based on the nominal (unshimmed) bearing clearance C. The average normalized shim thickness is defined as

$$\bar{\varepsilon}_S = \frac{1}{n_S} \sum_i \varepsilon_{S-i} \tag{11}$$

The optimization process itself is performed by coupling the integrated rotor-bearing model to a genetic algorithm [38], which has been successfully used in similar optimization problems [30,32]. Compared to gradient-based approaches, the advantage of evolutionary algorithms is that the search for solutions is global within the variable space and insensitive to the initial starting point. The optimization is started with 500 randomly selected individual solutions and stopped after 5000 evaluations. It is shown that this is sufficient to achieve good convergence.

Figure 9 presents the resulting Pareto curves for different structural damping coefficients. The results show that increasing the average shim leads to augmented rotordynamic performance, suggesting that selective shimming is a viable option for improved stability. Without structural damping, the minimum logarithmic decrement could be increased from -2.9 to -0.3. Also shown in the figure is that structural damping further enhances rotordynamic performance when coupled with selective shimming. As shown in the sensitivity analysis, this supports the observation that the effect of structural damping enhances stability at increased static loads (increased fluid film pressure rise). The selective shim pattern, which corresponds to the best rotordynamic performance, is summarized in Table 2.

Figure 10 compares the evolution of the critical mass of three individual bearing configurations: (a) the original reference bearing; (b) the original bearing with optimized shimming pattern (Table 1); and (c) the bearing with three equal shims as proposed by Kim and San Andrés [34]. At moderate compressibility, the optimum shim

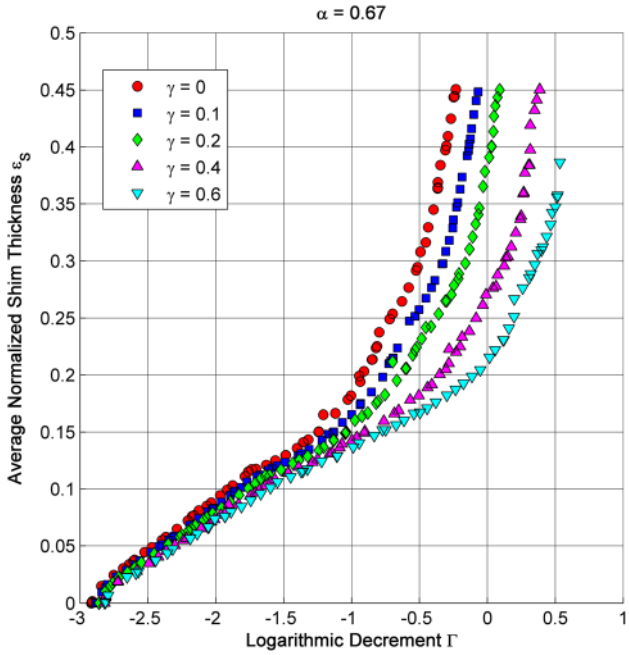

Fig. 9 Pareto curves for reference bearing (Table 1) for different structural damping γ

Table 2 Selective shim pattern for improved stability threshold for reference bearing (Table 1) operating at $\Lambda = 0.23$–2.3

Angular position ϕ_S (deg)	Normalized shim thickness ε_S (–)
0	0
72	0
144	0.9
216	0
288	0.9
360	0.9

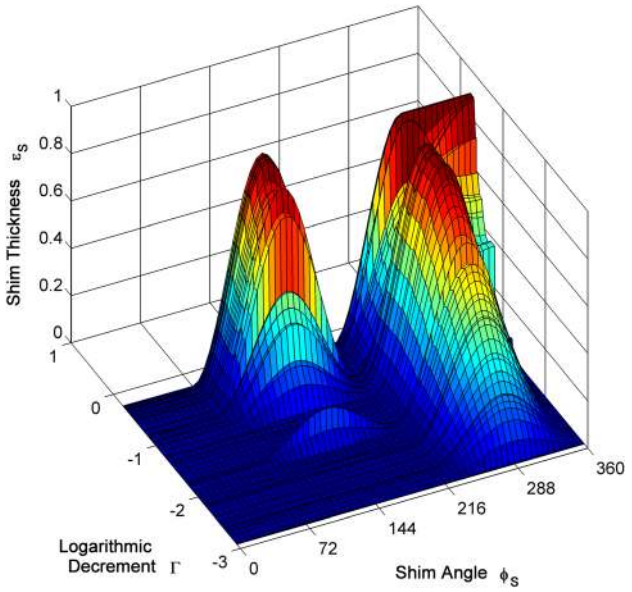

Fig. 11 Pareto-optimum shim distribution as a function of logarithmic decrement Γ for $\gamma = 0$, $\alpha = 0.67$

pattern improves the critical mass by more than two orders of magnitude compared to the original bearing. With selective shimming, the threshold rotational speed is increased by more than a factor 5 and 2.5 compared to the original and the 3-lobed configurations, respectively. Note that the estimated speed at instability onset ($\Lambda = 0.95$) agrees well with experimental data for the three equal shims pattern [34].

In summary, the results suggest that selective shimming is potentially an effective means to significantly improve the rotordynamic performance and the stability threshold of foil bearings. The evolution of the Pareto optimum shim patterns is shown in Fig. 11. The rotordynamic performance is first improved by gradually increasing the shim at 288 deg. For further improvement, an additional shim is added at 144 deg, and ultimately, a third shim is added near the top foil trailing edge. It can be shown that the

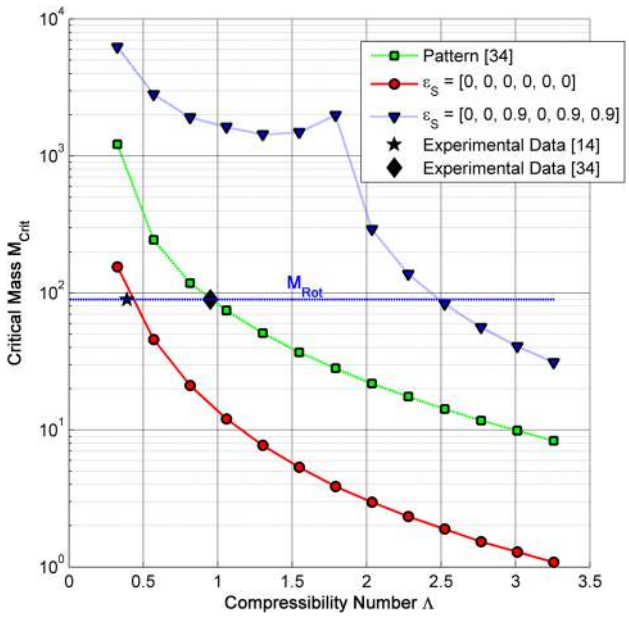

Fig. 10 Improvement in threshold speed at instability onset for: original reference bearing (solid); optimum selective shim pattern (dotted); and three equal shim pattern (Kim and San Andrés [34], dashed)

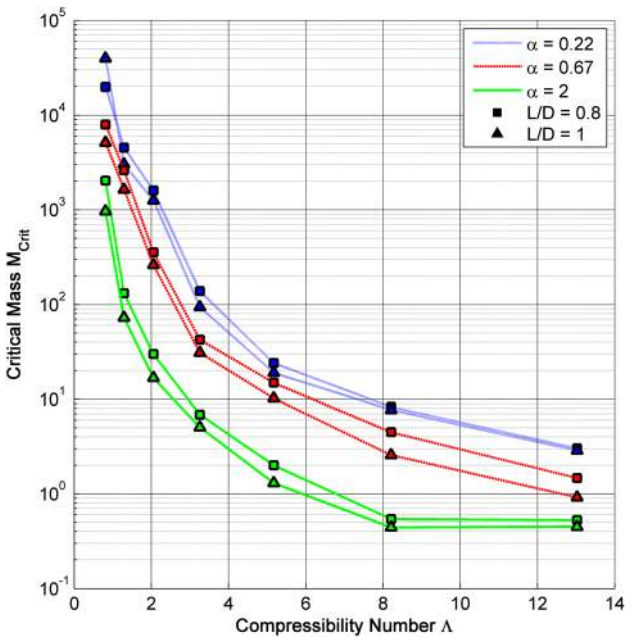

Fig. 12 Critical mass as a function of the highest operating compressibility number for optimized circumferential selective shim distributions

evolution of the optimum shim pattern does not depend on structural damping. Hence, it is suggested that optimization at one particular structural damping coefficient might be valid at other levels of damping.

Design Guidelines

The search for the optimum shim pattern described in the previous section was repeated for a typical range of bearing compliance, L/D ratios, and compressibility numbers. In a first attempt to define a set of unified design guidelines for stable, foil bearing-supported rotor operation, the optimization was performed assuming no structural damping. Figure 12 shows the resulting critical mass as a function of the highest operation compressibility number for each individual bearing with the best selective shim pattern. The results suggest that

(1) Shorter bearings ($L/D < 1$) seem to perform better, independent of the compressibility number. An inversion in trends occurs at low compressibility numbers and only for a compliance of 0.22.
(2) Increasing the bearing compliance decreases the rotordynamic performance independent of the bearing geometry and compressibility number
(3) The critical bearing mass increases with decreasing compressibility numbers

The key consequence is that shimmed foil bearings are preferably operated at low compressibility and low compliance, which corresponds to increased nominal bearing clearances. This is an interesting result, as bearing clearances are usually decreased to improve the stability of plain [39] or herringbone-grooved bearings [30]. The improved rotordynamic performance of shorter bearings is due to increased normalized loads and to reduced cross-coupled coefficients, which corroborates the results from the sensitivity analysis in Fig. 7.

The optimum selective shim patterns for the critical masses represented in Fig. 12 are plotted in Fig. 13 as a function of compressibility. Independent of the investigated bearing geometries, all patterns feature at least two shims, generating two distinct elevations in the circumferential direction. With increasing compressibility, the pattern of two individual elevations persists. The first elevation, however, is shifted towards the top foil leading edge, from 144 deg to 72 deg. It seems that the position shift of the first shim occurs at higher compressibility numbers with increasing bearing compliance. Increasing compressibility enhances, widens, and shifts the pressure rise across an aerodynamic wedge. It is therefore expected that at least one of the shims (aerodynamic wedge) shifts position as a function of compressibility to reduce the cross-coupled force contribution. With increased compliance, the aerodynamic effect of the wedge is reduced; thus, the shift towards the leading edge occurs at

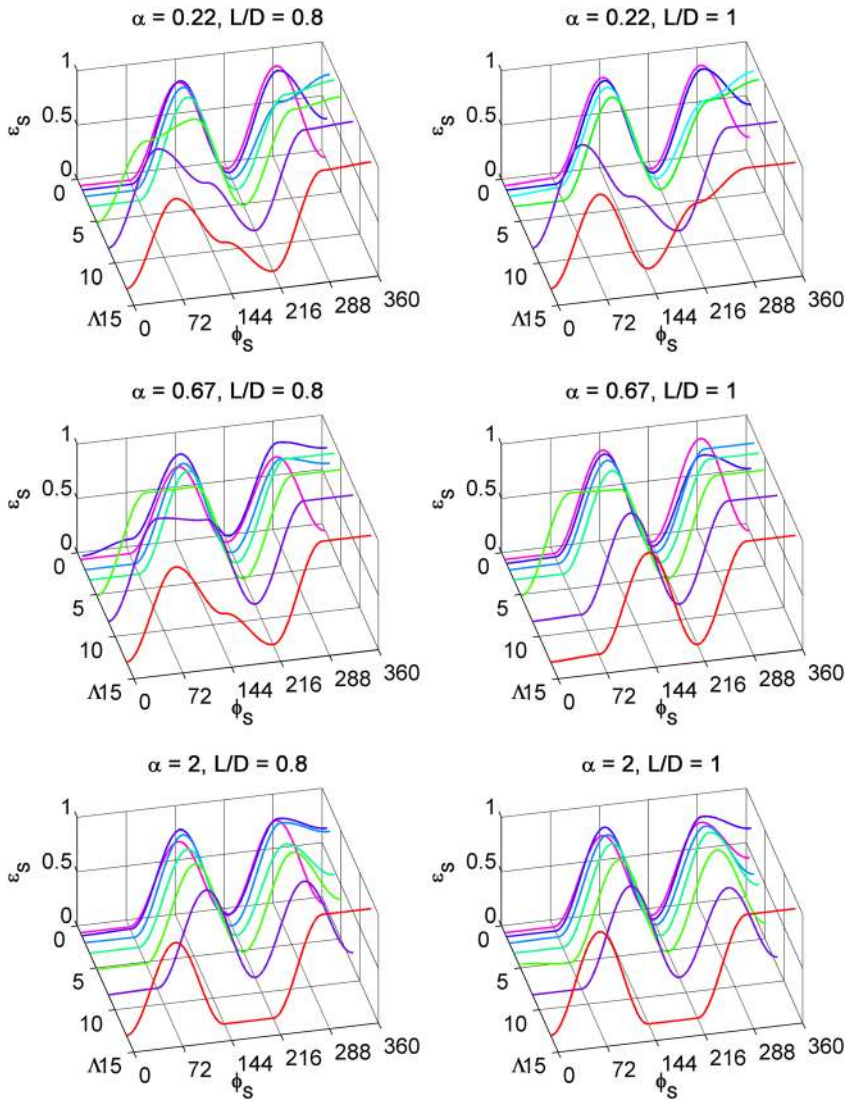

Fig. 13 Optimum selective shim patterns as a function of bearing compliance α, L/D ratio, and compressibility Λ

Table 3 Generalized selective shim pattern

Angular position ϕ_S (deg)	Normalized shim thickness ε_S (–)
0	0
72	0
144	0.9
216	0
288	0.9
360	0.5

higher compressibility. Note that, for low compressibility numbers, the optimum shimming pattern seems to vary only very little with bearing geometry. Therefore, operation at low compressibility seems to offer the opportunity to devise a general selective shim pattern that is independent of geometry. A generalized shim distribution is thus defined based on the average of optimum shim patterns at low compressibility numbers. This is summarized in Table 3. Figure 14 shows the resulting critical mass relative to that of the individual optimum shim pattern.

The lowest ratio between the two solutions is above 0.25, which is a reasonable compromise, given that selective shimming may increase the critical mass by more than two orders of magnitude. The penalty for using the generalized shim pattern compared to the optimum one does not seem to follow a pattern related to compliance, compressibility, or L/D ratio. The comparison also suggests that, although the optimum shim patterns vary little within the investigated bearing configurations operating at compressibility numbers lower than 2, the rotordynamic performance is very sensitive to the selective shim distribution. At high compressibility, the selective pattern performs well, except for $\alpha = 2$, where the critical mass ratio drops considerably (0.33). This is due to the combination of high compressibility (increased aerodynamic wedge effect) and the fact that, compared to the other cases, the generalized shim pattern differs considerably from the optimum pattern. Thus the generalized selective shim pattern may be used as a starting point if a sufficient rotordynamic margin is available. For more challenging situations, it is advisable to apply an appropriate optimized shim distribution.

General Design Guidelines. The results suggest that, to improve the rotordynamic performance, optimized selective shim patterns are most effective at compressibility numbers lower than approximately 5 and low bearing *L*/*D* ratios. For low bearing loads, small L/D ratios can be selected. Thus, the foil bearing design choice for a specific rotor speed and geometry is mostly governed by an appropriate choice of nominal bearing clearance and compliance. Note that compliance can be tuned by both the elastic foundation stiffness and the nominal bearing clearance.

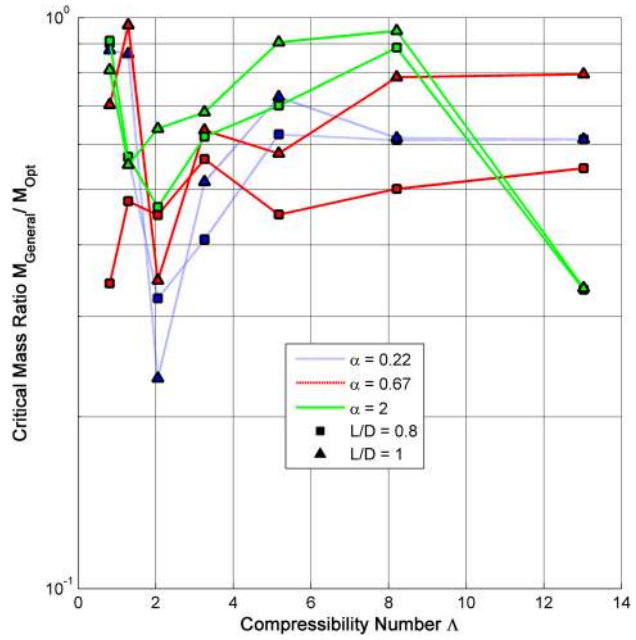

Fig. 14 Generalized selective shim pattern (Table 3) compared with individually optimized selective shim pattern

Adding compliance increases the tolerance to rotor misalignment due to assembly and manufacturing issues and allows the bearing to cope with significant thermal gradients and thermal expansions. In addition, the compliant support structure yields a bearing behavior, which temporarily allows overload and does not lead to instantaneous failure at large rotor orbits. This is a key advantage of compliant foil bearings over rigid surface bearings. However, as discussed previously, increased compliance reduces rotordynamic performance. Thus, a design compromise is required.

Assuming a known rotor geometry, the first step in defining the foil bearing design is to identify the nominal foil bearing clearance, which determines the nondimensional critical mass of the rotor and the bearing compressibility number. Using Fig. 12, an appropriate *L*/*D* ratio and a level of compliance for a sufficient stability margin can be selected. If a sufficient margin is available, the generalized selective shim pattern may be applied. If the design constrains are more challenging, Fig. 13 can be used to determine the optimum shim distribution for the specific bearing design and operating conditions. In cases where the rotor mass exceeds the critical foil bearing mass, the only remedy to avoid subsynchronous whirl is to further decrease the L/D ratio and/or to increase the bearing diameter, both leading to significant rotor design modifications. This suggests that the design of the rotor-bearing system is strongly coupled and thus calls for an integrated design approach (see, for example, Schiffmann and Favrat [30]). Although digital number values in excess of 4×10^6 mm-rpm seem feasible with foil bearings [10], increased windage losses at large bearing diameters may lead to a challenging thermal management, which needs to be carefully considered as well.

Summary and Conclusions

A reduced order foil bearing model, coupled with a rigid-body, linear rotordynamic model, was used to investigate the underlying rotordynamic mechanisms and the onset speed of instability of a foil bearing-supported rotor. Introducing a critical mass parameter as a measure for stability, a criterion for the whirl instability onset was proposed. This model was implemented for a rotor with published experimental data. The computation suggests that the whirl onset speed is accurately predicted by the reduced order model.

A sensitivity analysis demonstrates that structural damping does not significantly alter the onset of subsynchronous whirl. It is shown, however, that the orientation of the axial feed line of the top foil can strongly influence the bearing load capacity and rotordynamic performance.

The analysis further indicates that the static fluid film pressure distribution governs rotordynamic stability. Selective shimming is introduced to tailor the unperturbed pressure distribution for improving rotordynamic performance. The selective shim pattern is found via multiobjective optimization using the integrated foil bearing-supported rotor model. It is shown that, with an optimally shimmed foil bearing, the critical mass parameter can be improved by more than two orders of magnitude.

The optimum shim patterns are summarized for a variety of foil bearing geometries with different *L*/*D* ratios (0.8–1), compliance (0.22, 0.67, 2), and compressibility (0.2–13.5) in a first attempt to establish general guidelines for stable foil bearing design. The results demonstrate that shimmed foil bearings are preferably operated at low compressibility and low compliance, i.e., at large nominal clearance and at low *L*/*D* ratios. It is shown that the optimum selective shim distribution varies little with geometry at compressibility numbers lower than 2, such that a generalized selective shim pattern can be introduced. Compared to the

optimized shim patterns, the generalized shim pattern reduces the critical mass by approximately a factor of 4. This suggests a considerable improvement compared to unshimmed bearings. It is also shown that the rotordynamic performance is sensitive to the selective shim distribution and that experimental fine-tuning is necessary when finalizing the foil bearing design.

Acknowledgment

The authors would like to thank Professor L. San Andrés for the useful discussions, helpful comments, and insights on foil bearings.

Nomenclature

$[C]$ = system damping matrix
C = nominal bearing clearance (m)
D = rotor diameter (m)
e_s = shim thickness (m)
$F_0 = f/(p_a LD)$, normalized static bearing load
f = static bearing load (N)
$H = h/C$, normalized bearing clearance
h = fluid film thickness (m)
I_{Crit} = normalized critical rotor inertia
J_P = polar rotor inertia (kgm^2)
J_T = transverse rotor inertia (kgm^2)
(K) = system stiffness matrix
K_B = structural support stiffness per unit area (Nm^{-3})
L = bearing length (m)
l = distance between journals (m)
$l_{a/b}$ = journal position relative to center of gravity (m)
(M) = system inertia matrix
M_{Crit} = normalized critical rotor mass
M_{Rot} = normalized rotor mass
m_{Rot} = rotor mass (kg)
n_S = number of shims
$P = p/p_a$, normalized pressure
p = pressure (Pa)
p_a = ambient pressure (Pa)
q = normalized system motion vector
R = rotor radius (m)
s = rotordynamic system eigenvalue (s^{-1})
u = real part of z (Nm^{-1})
v = imaginary part of z (Nm^{-1})
Z = system impedance (Nm^{-1})
z = system impedance eigenvalue (Nm^{-1})

Greek symbols

$\alpha = p_a/(\text{CK}_B(1+\gamma))$, bearing compliance
$\varepsilon_s = e_s/C$, normalized shim thickness
$\varepsilon_{x,y}$ = normalized rotor eccentricity
ϕ_S = shim angle (deg)
Γ = logarithmic decrement
γ = structural bearing damping
$\Lambda = 6\mu\omega_{\text{Rot}}/p_a \cdot (R/C)^2$, compressibility number
λ = real part of s (s^{-1})
μ = viscosity (Pas)
Ω = whirl ratio
Ω_{Crit} = whirl ratio at instability onset
ω_{Rot} = rotator speed (s^{-1})
ω_{EX} = excitation speed (s^{-1})
ω = imaginary part of s (s^{-1})
$\sigma = 12\mu\Omega\omega_{\text{Rot}}/p_a \cdot (R/C)^2$, squeeze film number
θ_F = attitude angle (deg)
τ = normalized time
$\zeta = l_a/(l_a+l_b)$, relative rotor center of gravity

Subscripts

z = axial component
θ = circumferential component
CYL = cylindrical rotor motion
CON = conical rotor motion
$x0$ = static rotor displacement component in x
y0 = static rotor displacement component in y

References

[1] Agrawal, G. L., 1997, "Foil Air/Gas Bearing Technology—An Overview," ASME Paper No. 1997-GT-347.
[2] Moore, J. J., Lerche, A., Allison, T., Ransom, D. L., and Lubell, D., 2010, "Development of a High Speed Gas Bearing Test Rig to Measure Rotordynamic Force Coefficients," ASME Paper No. GT2010-23217.
[3] Lubell, D. R., Wade, J. L., Chauhan, N. S., and Nourse, J. G., 2008, "Identification and Correction of Rotor Instability in an Oil-Free Gas Turbine," ASME Paper No. GT2008-50305.
[4] Hou, Y., Zhu, Z. H., and Chen, C. Z., 2004, "Comparative Test on Two Kinds of New Compliant Foil Bearing for Small Cryogenic Turbo-Expander," Cryogenics, **44**, pp. 69–72.
[5] Heshmat, H., 1994, "Advancement in the Performance of Aerodynamic Foil Journal Bearings: High Speed and Load Capability," ASME J. Tribol., **116**, pp. 287–295.
[6] Lubell, D., Corte, C. D., and Stanford, M., 2006, "Test Evolution and Oil-Free Engine Experience of a High Temperature Foil Air Bearing Coating," ASME Paper No. GT2006-90572.
[7] Heshmat, H., 2000, "Operation of Foil Bearings Beyond the Bending Critical Mode," ASME J. Tribol., **122**, pp. 192–198.
[8] Walton, J. F., and Heshmat, H., 2002, "Application of Foil Bearings to Turbomachinery Including Vertical Operation," ASME J. Eng. Gas Turbines Power, **124**, pp. 1032–1041.
[9] Kim, T. H., Lee, J., Kim, C. H., and Lee, Y. B., 2010, "Rotordynamic Performance of an Oil-Free Turbocharger Supported on Gas Foil Bearings: Effects of an Assembly Radial Clearance," ASME Paper No. GT2010-23243.
[10] Heshmat, H., Saphiro, W., and Gray, S., 1982, "Development of Foil Journal Bearings for High Load Capacity and High Speed Whirl Stability," ASME J. Lubr. Technol., **104**(2), pp. 149–156.
[11] Lee, Y., Kim, T., Kim, C., Lee, N., and Choi, D., 2004, "Dynamic Characteristics of a Flexible Rotor System Supported by a Viscoelastic Foil Bearing," Tribol. Int., **37**, pp. 679–687.
[12] San Andrés, L., Chirathadam, T. A., and Kim, T. H., 2010, "Measurement of Structural Stiffness and Damping Coefficients in a Metal Mesh Foil Bearing," ASME J. Eng. Gas Turbines Power, **132**, p. 032503.
[13] San Andrés, L., and Chirathadam, T. A., 2010, "Identification of Rotordynamic Force Coefficients of a Metal Mesh Foil Bearing Using Impact Load Excitations," ASME Paper No. GT2010-22440.
[14] San Andrés, L., and Kim, T. H., 2008, "Forced Nonlinear Response of Gas Foil Bearing Supported Rotors," Tribol. Int., **41**, pp. 704–715.
[15] Rubio, D., and San Andrés, L., 2006, "Bump-Type Foil Bearing Structural Stiffness: Experiments and Predictions," ASME J. Eng. Gas Turbines Power, **128**, pp. 653–660.
[16] Kim, T. H., and San Andrés, L., 2006, "Limits for High-Speed Operation of Gas Foil Bearings," ASME J. Tribol., **128**, pp. 670–673.
[17] Kim, T. H., and San Andrés, L., 2008, "Heavily Loaded Gas Foil Bearings: A Model Anchored to Test Data," ASME J. Eng. Gas Turbines Power, **130**, p. 012504.
[18] Pan, C. H. T., 1964, "Spectral Analysis of Gas Bearing Systems for Stability Studies," MTI Technical Report No. 64TR58.
[19] Pan, C. H. T., and Kim, D., 2007, "Stability Characteristics of a Rigid Rotor Supported by a Gas-Lubricated Spiral-Groove Conical Bearing," ASME J. Tribol., **129**, pp. 375–383.
[20] Heshmat, H., Walowit, J. A., and Pinkus, O., 1983, "Analysis of Gas-Lubricated Foil Journal Bearings," ASME J. Lubr. Technol., **105**, pp. 647–655.
[21] Kim, T. H., and San Andrés, L., 2007, "Analysis of Advanced Gas Foil Bearings With Piecewise Linear Elastic Supports," Tribol. Int., **40**, pp. 1239–1245.
[22] San Andrés, L., and Kim, T. H., 2009, "Analysis of Gas Foil Bearings Integrating FE Top Foil Models," Tribol. Int., **42**, pp. 111–120.
[23] Carpino, M., and Talmage, G., 2003, "A Fully Coupled Finite Element Formulation for Elastically Supported Foil Journal Bearings," STLE Tribol. Trans., **46**, pp. 560–565.
[24] Carpino, M., and Talmage, G., 2006, "Prediction of Rotor Dynamic Coefficients in Gas Lubricated Foil Journal Bearings With Corrugated Sub-Foils," STLE Tribol. Trans., **49**, pp. 400–409.
[25] Ruscitto, D., Cormick, J. M., and Gray, S., 1978, "Hydrodynamic Air Lubricated Compliant Surface Bearing for an Automotive Gas Turbine Engine I—Journal Bearing Performance," NASA Technical Report No. CR-135368.
[26] Faria, M. T. C., and San Andrés, L., 2000, "On the Numerical Modeling of High-Speed Hydrodynamic Gas Bearings," ASME J. Tribol., **122**, pp. 124–130.
[27] Faria, M. T. C., 2001, "Some Performance Characteristics of High Speed Gas Lubricated Herringbone Groove Journal Bearings," JSME Int. J., Ser. C, **44**, pp. 775–781.
[28] Rubio, D., and San Andrés, L., 2007, "Structural Stiffness, Dry Friction Coefficient, and Equivalent Viscous Damping in a Bump-Type Foil Gas Bearing," ASME J. Eng. Gas Turbines Power, **129**, pp. 494–502.
[29] Kim, T. H., and San Andrés, L., 2009, "Effect of Side Feed Pressurization on the Dynamic Performance of Gas Foil Bearings: A Model Anchored to Test Data," ASME J. Eng. Gas Turbines Power, **130**, p. 012501.
[30] Schiffmann, J., and Favrat, D., 2010, "Integrated Design and Optimization of Gas Bearing Supported Rotors," ASME J. Mech. Des., **132**, p. 051007.

[31] Schiffmann, J., and Favrat, D., 2009, "Experimental Investigation of a Direct Driven Radial Compressor for Domestic Heat Pumps," Int. J. Refrig., **32**, pp. 1918–1928.
[32] Schiffmann, J., and Favrat, D., 2010, "The Effect of Real Gas on the Properties of Herringbone Grooved Journal Bearings," Tribol. Int., **43**, pp. 1602–1614.
[33] Lund, J. W., 1968, "Calculation of Stiffness and Damping Properties of Gas Bearings," ASME J. Lubr. Technol., **90**, pp. 783–803.
[34] Kim, T. H., and San Andrés, L., 2009, "Effects of a Mechanical Preload on the Dynamic Force Response of Gas Foil Bearings: Measurements and Model Predictions," STLE Tribol. Trans., **52**, pp. 569–580.
[35] San Andrés, L., Rubio, D., and Kim, T. H., 2007, "Rotordynamic Performance of a Rotor Supported on Bump Type Foil Gas Bearings: Experiments and Predictions," ASME J. Eng. Gas Turbines Power, **129**, pp. 850–857.
[36] Kim, D., Creary, A., Chang, S. S., and Kim, J. H., 2009, "Mesoscale Foil Gas Bearings for Palm-Sized Turbomachinery: Design, Manufacturing, and Modeling," ASME J. Eng. Gas Turbines Power, **131**, p. 042502.
[37] Sim, K., Lee, Y., Kim, T. H., and Lee, J., 2012, "Rotordynamic Performance of Shimmed Gas Foil Bearings for Oil-Free Turbochargers," ASME J. Tribol., **134**, p. 031102.
[38] Molyneaux, A., Leyland, G. B., and Favrat, D., 2010, "Environomic Multi-Objective Optimization of a District Heating Network Considering Centralized and Decentralized Heat Pumps," Energy, **35**, pp. 751–758.
[39] Ng, C. W., 1965, "Linearized Ph Stability Theory for Finite Length, Self-Acting Gas-Lubricated, Plain Journal Bearings," J. Basic Eng., **87**, pp. 559–567.